Intrinsically Zirconium-89-Labeled Manganese Oxide Nanoparticles for *In Vivo* Dual-Modality Positron Emission Tomography and Magnetic Resonance Imaging

Yonghua Zhan[1,†], Emily B. Ehlerding[2,†], Sixiang Shi[3], Stephen A. Graves[2], Shreya Goel[3], Jonathan W. Engle[2], Jimin Liang[1,*], and Weibo Cai[2,3,*]

[1] *Engineering Research Center of Molecular and Neuro Imaging of the Ministry of Education, School of Life Science and Technology, Xidian University, Xi'an, Shaanxi, 710071, China*
[2] *Department of Medical Physics, University of Wisconsin-Madison, WI, 53705, USA*
[3] *Department of Radiology, University of Wisconsin-Madison, WI, 53705, USA*

Manganese-based nanoparticles (NPs) have recently attracted much attention in the field of biomedical imaging due to their impressive enhanced T_1 contrast ability. Although the reported manganese-based NPs have exhibited good imaging capabilities as contrast agents, it is still urgent to develop novel multifunctional manganese-based imaging probes for future biomedical imaging, especially PET/MRI probes. Herein, we present chelator-free zirconium-89 (^{89}Zr, $t_{1/2}$: 78.4 h) labeling of manganese oxide NPs (Mn$_3$O$_4$@PEG) with ~78% labeling yield and good stability. Serial positron emission tomography (PET) and magnetic resonance imaging (MRI) studies non-invasively assessed the biodistribution patterns of the NPs and the feasibility of *in vivo* dual-modality imaging and lymph-node mapping. Since Mn$_3$O$_4$ NPs exhibited desirable properties for enhanced T_1 imaging and the simplicity of chelator-free radiolabeling, [^{89}Zr]Mn$_3$O$_4$@PEG NPs offer a novel, simple, safe and accurate nanoplatforms for future precise cancer imaging and diagnosis.

KEYWORDS: *Manganese Oxide Nanoparticles, Positron Emission Tomography, Magnetic Resonance Imaging, Zirconium-89, Chelator-Free.*

INTRODUCTION

In the past decades, molecular imaging techniques have demonstrated great value in the early detection and diagnosis of disease, which is attributed to their fast and accurate diagnostic abilities at the molecular and cellular levels.[1–3] Among them, the integration of PET and MRI has been under rapid development and is currently in clinical trials for applications in cancer detection and diagnosis due to the very high sensitivity of PET and the ultra-high spatial resolution of MRI.[4,5] To take advantage of the hybrid PET/MRI imaging technology, design and synthesis of novel multifunctional PET/MRI nanoprobes has been a hot research topic since their emergence in the last decade.[6–8] As one half of the PET/MRI nanoprobes, current MRI contrast agents are commonly in the forms of T_1-positive contrast agents and T_2-negative contrast agents.[9] In particular. T_2 contrast agents based on superparamagnetic iron oxide NPs (SPIONs) have been widely used as the MRI contrast component in PET/MRI probes over the last two decades and a few have advanced into clinical trials or received the approval of the Food and Drug Administration (FDA) of the United States.[10–12] However, these magnetic-based PET/MRI nanoprobes have been somewhat limited in clinical applications due to their drawbacks of signal-decreasing effects and high susceptibility. Therefore, it is desirable to develop novel PET/MRI nanoprobes with higher T_1 or T_2 relaxivity to meet the future clinical requirements.

Recently, manganese-based NPs have emerged as a new class of T_1-weighted contrast agents thanks to their relatively high magnetization spins and fast water proton exchange rates.[13] Meanwhile, manganese-based agents also exhibit good biocompatibility and low side effects because manganese itself is an essential component of

cells and a cofactor for many metabolic enzymes, which is attributed to the dissolution of the manganese oxide nanocrystal at low pH.[13, 14] Most importantly, manganese-based NPs with good crystallinity and uniformity have been demonstrated to be easily synthesized on a large scale under mild and ambient reaction conditions.[15] This new promising class of MRI contrast agents, particularly manganese oxides, opens a new direction in biomedical imaging and tumor-targeted diagnosis for future medicine.[14, 16] Progress in developing multimodality imaging probes and their applications in biomedical imaging have been reported in recent years. For example, solid and hollow MnO-based T_1 NP contrast agents have been reported for selectively imaging breast cancer cells and for drug delivery by several groups.[17–22] Yang and co-workers further developed silica-coated Mn_3O_4 core–shell NPs for tumor folate-receptor-targeted MRI and fluorescent imaging *in vitro* and tumor aptamer-receptor-targeted MRI imaging *in vivo*.[23–25] Despite many desirable properties for biomedical applications, there are currently few reports related to the fusion of PET tracers (radionuclides) and manganese oxide-based T_1 contrast agents into one single probe for *in vivo* biomedical imaging. Therefore, it is of vital importance to develop novel dual-modality PET/MRI imaging probes based on manganese oxide NPs.

Chelator-based methods have been largely employed for radiolabeling NPs in the past. For example, by using NOTA (1,4,7-triazacyclononane-1,4,7-triacetic acid), DOTA(1,4,7,10-tetraazacyclododecane-1,4,7,10-tetraacetic acid), or desferrioxamine B (DFO) as the chelator, Cu-64 and Zr-89 have been use to label graphene oxide,[26] SPIONs,[12] mesoporous silica NPs,[27] and monocolonal antibodies (mAb),[28] for preclinical studies. However, potential dissociation of these radionuclides from NPs could easily lead to false interpretation of PET imaging results *in vivo*. For example, significant bladder and bone uptake have been observed during *in vivo* PET imaging of ^{64}Cu-DOTA-Au@PEG NPs[29] and [89]Zr-DFO-mAb[30–32] respectively, indicating that the radionuclides dissociated from their respective chelator. To address this concern, recent successful syntheses of intrinsically radiolabeled NPs (i.e., without the use of a chelator) have been reported, such as ^{64}Cu-labeled porphysomes[33] and CuS NPs,[34] [72]As and [69]Ge-labeled SPIONs,[35, 36] and [89]Zr-labeled mesoporous silica NPs,[37] Gd_2O_2S:Eu NPs, and WS2/WOx nanodots.[38–40] These NPs have exhibited great potential in providing a facile, faster, more stable, and more specific radiolabeling technique for future clinical applications. Inspired by these successes, we were encouraged to develop radio-labeled NPs with manganese oxide-based T_1 contrast components for *in vivo* biomedical applications.

In this work, we hypothesized that mixing suitable water-soluble manganese oxide NPs with [89]Zr would yield [89]Zr-labeled manganese oxide ([[89]Zr]Mn_3O_4@PEG) NPs
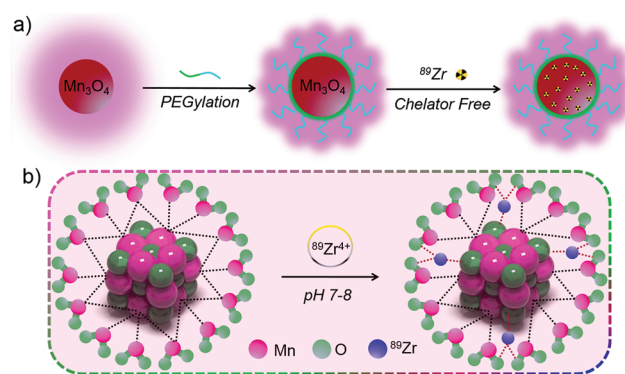
Scheme 1. The synthetic process of [[89]Zr]Mn_3O_4@PEG NPs.

because of the specific affinity of [89]Zr for the manganese oxide surface (Scheme 1).[37–40] Subsequently, systematic *in vivo* PET/MRI imaging, biodistribution, and lymph node mapping studies were carried out in normal healthy BALB/c mice to evaluate their potential capabilities as novel dual-modality PET/MRI agents, and further validated through various *in vitro* and *ex vivo* experiments. Moreover, serum biochemistry assays and histological assessments were also carried out to determine the potential toxicity of these NPs.

EXPERIMENTAL SECTION

Materials

Oleylamine (technical grade 90%), oleic acid (technical grade 90%), xylene (98%), manganese (II) acetate (98%), and the CCK-8 assay were all purchased from Sigma-Aldrich. DSPE-PEG$_{5000}$-NH$_2$ was purchased from Creative PEGworks (Winston Salem, NC). PD-10 desalting columns was acquired from GE Healthcare. All buffers and water were of Millipore grade. All chemicals were used as received without further purification.

Characterization

The size and morphology of Mn_3O_4 NPs were observed using an FEI T12 transmission electron microscope (TEM) operated at an accelerating voltage of 120 kV. X-ray diffraction (XRD) measurements were performed on a Bruker D8 diffractometer with Cu Kα radiation ($\lambda =$ 0.15405 nm). The surface zeta potential and hydrodynamic size were measured using a Malvern Zetasizer Nano ZS. The T_1-relaxivities were measured and T_1-weighted images were acquired with a conventional spin echo acquisition (repetition time, TR, 1000 ms) with echo time, TE, of 50 ms, and a section thickness of 1 mm in a 7 T Bruker Micro-MR small animal scanner. Relaxivity values of r_1 were calculated through curve fitting of $1/T_1$ relaxation time (s^{-1}) versus the Mn concentration (mM).

Synthesis of the Mn$_3$O$_4$@PEG NPs

Mn_3O_4 NPs were prepared according to a previously reported method with slight modifications.[14] In brief,

manganese (II) acetate (1 mmol, 0.17 g) and a mixture of oleic acid (2 mmol, 0.57 g) and oleylamine (10 mmol, 2.67 g) were dissolved in 15 mL of xylene in air atmosphere. After slowly heating to 95 °C, 1 mL of DI water was injected into the solution under brisk stirring, and the resulting solution was aged at 95 °C for 3 h. A total of 100 mL of ethanol was then added to precipitate the nanocrystals, followed by centrifugation to retrieve the nanocrystals in powder form. 10 mg of Mn_3O_4 nanocrystals were dispersed in 1 mL of chloroform and then added to 20 mg of DSPE-PEG$_{5000}$-NH$_2$ in 2 mL chloroform. After stirring for 2–3 h at 25 °C and evaporating the solvent by argon blowing, the residue was kept at 60 °C in vacuum for 30 min. Upon the addition of 15 mL of DI water, a transparent brown solution was generated after sonication for 15 min. After filtration by centrifugation 3 or 4 times, excess DSPE-PEG$_{5000}$-NH$_2$ was removed and Mn_3O_4@PEG NPs were obtained.

[89]Zr Labeling and Serum Stability Studies

[89]Zr-oxalate was produced by the University of Wisconsin-Madison cyclotron group. Briefly, a natural yttrium-89 ([89]Y) foil (250 μm, 99.9%) was irradiated with a proton beam to create [89]Zr via the [89]Y (p, n) [89]Zr reaction by using a 16 MeV GE PETtrace cyclotron. After isotope separation and purification, [89]Zr-oxalate was obtained with a specific activity of >20 GBq/μmol. 200 μL of Mn_3O_4@PEG NPs (1 mg/mL) in HEPES buffer (0.1 M, pH 7.5) was mixed with [89]Zr-oxalate at 75 °C. The final pH value of the mixture was adjusted to 7–8 by using 2 M Na_2CO_3. [89]Zr labeling yield was monitored and quantified at different time points (from 3 min to 3 h) by using thin layer chromatography (TLC) and a final labeling time of 1 h was selected. The [[89]Zr]Mn_3O_4@PEG NPs could be easily collected by centrifugation at 15,000 rpm for 5 min. To ensure that [[89]Zr]Mn_3O_4@PEG NPs were sufficiently stable for *in vivo* applications, serum stability studies were carried out. [[89]Zr]Mn_3O_4@PEG NPs were incubated in complete mouse serum at 37 °C for up to 48 h, and analysis was performed as previously described.[38] The percentage of retained [89]Zr on the [[89]Zr]Mn_3O_4@PEG NPs was calculated according to the equation [(total radioactivity-radioactivity in filtrate)/total radioactivity] × 100%.

Cell Cytotoxicity Studies of Mn_3O_4@PEG NPs

The cytotoxicity of Mn_3O_4@PEG NPs was assessed with a CCK-8 assay using SGC-7901 cells and HEK-293 cells. Briefly, cells were seeded in 96-well plates at 20,000 cells per well in 200 μL culture medium. The cells were maintained in RPMI-1640 containing 10% fetal bovine serum (FBS) and incubated at 37 °C in a humidified cell culture incubator with 5% CO_2 atmosphere for 24 h. Mn_3O_4@PEG NP solutions with different concentrations from 200 to 1000 μg/mL were added to each well, and the cells were subjected to a CCK-8 assay after being

incubated for another 24 h. The cell viability was determined through measuring the absorption at 450 nm using a microplate reader. Cell viability was calculated using: cell viability (%) = (mean absorption value of treatment group/mean absorption value of control) × 100.

In Vivo Toxicity Studies of Mn_3O_4@PEG NPs

The toxicity of Mn_3O_4@PEG NPs to healthy male BALB/c mice was evaluated through injecting Mn_3O_4@PEG NPs (dose: 20 mg/kg) via the tail vein. Mice injected with only PBS served as a control group ($n = 3$). Three mice were sacrificed to collect blood for serum biochemistry assays on both day 7 and day 14 post-injection. At the same time, major organs from each mouse were harvested and fixed in 4% paraformaldehyde solution for 1 day. These tissues were then embedded in paraffin and stained with hematoxylin and eosin (H&E) and examined using a digital microscope (Leica DM5000). Examined tissues included the heart, liver, spleen, lung, and kidney. The serum chemistry data, including hepatic and kidney function markers, was measured by the University of Wisconsin-Madison Veterinary Hospital.

In Vivo PET/MRI Imaging and Biodistribution Studies

PET scans of BALB/c mice ($n = 3$ per group) at 0.5, 2, 12, and 48 h post-injection (p.i.) of [[89]Zr]Mn_3O_4@PEG NPs (~100 μCi or 2.7 MBq) were performed using an Inveon rodent model microPET/microCT scanner (Siemens Medical Solutions USA, Inc.) following tail vein injection. Detailed procedures for data acquisition and analysis of the PET data have been reported previously.[38] Quantitative data are presented as percentage injected dose per gram of tissue (%ID/g). For *in vivo* lymph node mapping with PET, 40 μL of [[89]Zr]Mn_3O_4@PEG NPs (~60 μCi or 0.81 MBq) was subcutaneously injected into the left footpad of healthy BALB/c mice. Time points of 0.5 h, 2 h and 6 h were selected for serial PET scans. *In vivo* T_1-weighted MR imaging was performed at 0.5 h, 2 h and 6 h post-injection after intravenous injection of 200 μL Mn_3O_4@PEG with a Mn concentration of 1 mM and used a 7 T small animal scanner (Agilent Technologies, Santa Clara, CA) with the following parameters: TR = 500 ms; TE = 12 ms; flip angle = 120°; FOV = 40 mm × 40 mm; matrix = 256 × 256; NEX = 8; slice thickness = 1 mm for axial liver images and 0.5 mm for coronal and cross lymph node mapping. All the animal studies were conducted under a protocol approved by the University of Wisconsin Institutional Animal Care and Use Committee.

RESULTS AND DISCUSSION
Synthesis and Characterization

As shown in Scheme 1, [[89]Zr]Mn_3O_4@PEG NPs were prepared uising similar methods to those we have previously
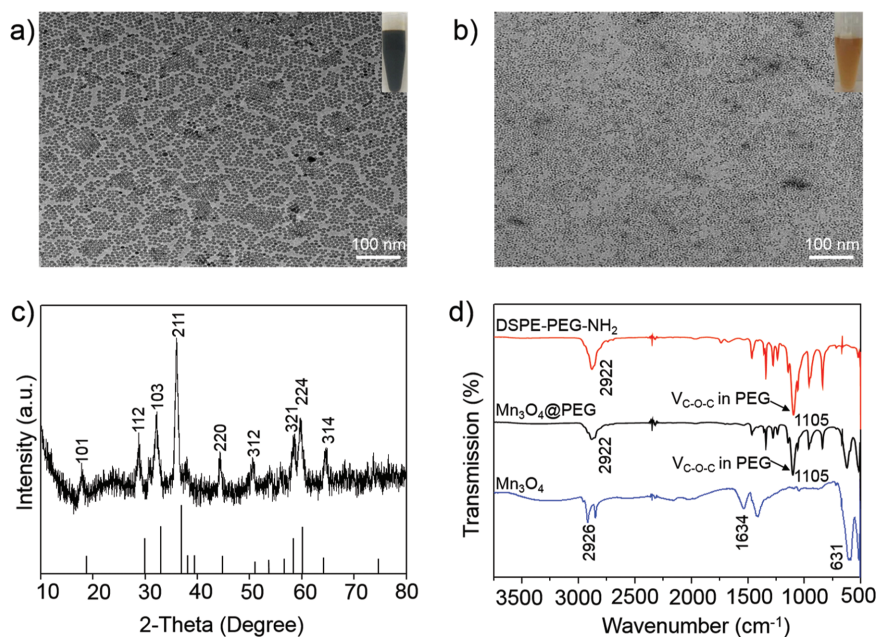
Figure 1. Characterization of Mn₃O₄@PEG NPs. (a) TEM images of Mn₃O₄; (b) TEM images of Mn₃O₄@PEG; (c) X-ray diffraction pattern of Mn₃O₄ NPs; (d) The FT-IR spectrum of DSPE-PEG-NH₂ (red line), Mn₃O₄ (blue line) and Mn₃O₄@PEG (black line).

reported.[37, 38] The uniform Mn_3O_4 NPs were monodispersed in nonpolar organic solvent (Fig. 1(a), inset) and had a small spherical shape of approximately 8 nm, which was consistent with previous reports.[14, 24, 25] Furthermore, the hydrophobic Mn_3O_4 NPs were successfully transferred to the aqueous phase through coating with amine-functionalized PEG lipids (DSPE-PEG$_{5000}$-NH$_2$) and showed good stability in aqueous solution (Fig. 1(b), inset). In addition, DLS measurements showed that Mn_3O_4@PEG had a hydrodynamic diameter of 10 ± 3.5 nm, similar to the observation from TEM. Meanwhile, the zeta-potential value of Mn_3O_4@PEG (23.7 ± 3.5 mV) further verified the existence of the NH$_2$ group. Meanwhile, the stability of Mn_3O_4@PEG NPs was also investigated in PBS and 10% FBS at different temperatures. The results indicated that the particle size of the Mn_3O_4@PEG NPs did not change significantly after two weeks in different media. Figure 1(c) shows the XRD pattern of the Mn_3O_4 NPs. Clearly, all the diffraction peaks of the as-prepared Mn_3O_4 NPs can be indexed as a tetragonal Mn_3O_4 phase (Joint Committee for Powder Diffraction Standards (JCPDS) card no: 24-0734) without metallic manganese or other oxide phase, which indicates that the as-synthesized Mn_3O_4 NPs are crystalline and of high purity.

Further investigation of the FT-IR spectra of these NPs confirmed the presence of PEG on the surface of Mn_3O_4 NPs (Fig. 1(d)). The sample exhibited a strong band around $\nu = 1105$ cm^{-1}, corresponding to the C–O–C asymmetric (ν_{as}) stretching vibration. To examine the effectiveness of the Mn_3O_4 NPs as positive MRI contrast agents, the relaxation properties of Mn_3O_4 NPs in aqueous

media were measured by a 7 T MRI scanner. It was clear that Mn_3O_4@PEG NPs displayed signal enhancement in the T_1-weighted MR images with increasing Mn concentration (Fig. 2(a)). The r_1 value of the Mn_3O_4@PEG NPs was calculated from the linear fitting of the measured $1/T_1$ data versus Mn^{2+} concentration as 0.58 mM^{-1}s^{-1} (Fig. 2(b)). These values are also similar to those of previously reported Mn_3O_4 NPs, verifying their potential use as a positive MRI contrast agent.[20, 23–25]
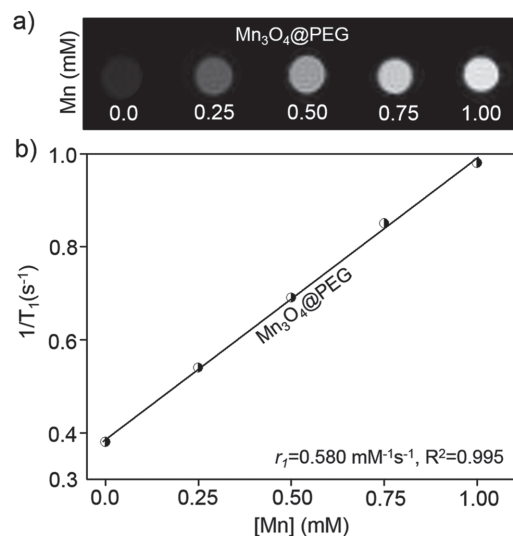
Figure 2. The relaxation properties of Mn₃O₄@PEG NPs. (a) T_1-weighted MR imaging of Mn₃O₄@PEG NPs; (b) T_1 relaxivity plot of aqueous suspensions of Mn₃O₄@PEG NPs on a 7 T MRI system.
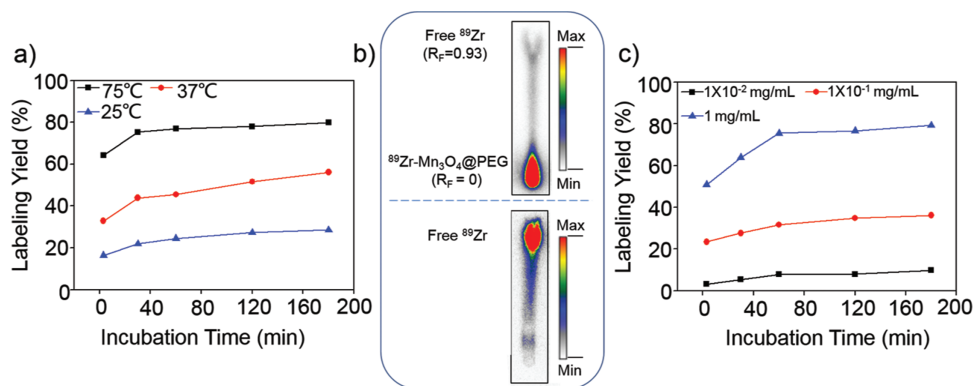
Figure 3. Radiolabeling yield of [^{89}Zr]Mn$_3$O$_4$@PEG NPs. (a) Time-dependent ^{89}Zr labeling yields of [^{89}Zr]Mn$_3$O$_4$@PEG with varied temperature; (b) Autoradiography of TLC plates of [^{89}Zr]Mn$_3$O$_4$@PEG (top) and free ^{89}Zr (bottom); (c) ^{89}Zr labeling yields of [^{89}Zr]Mn$_3$O$_4$@PEG with varied concentrations.

Chelator-Free ^{89}Zr-Labeling and Serum Stability Studies

Inspired by our previous reports on the intrinsic radiolabeling of ^{89}Zr to mesoporous silica NPs and Gd$_2$O$_2$S:Eu@PEG NPs,[37, 38] and *As and ^{69}Ge to iron oxide NPs,[35, 36] we reasonably postulated that [^{89}Zr]Mn$_3$O$_4$@PEG could be easily formed because of the strong and specific affinity of ^{89}Zr for the Mn$_3$O$_4$ surface, which was possible attributhed to the formation of Zr complexes occupy vacant Mn$_3$O$_4$ tetrahedral sites on the octahedrally terminaged surface of the magnetite NPs (Scheme 1(b)).[37] After mixing water-soluble Mn$_3$O$_4$@PEG with ^{89}Zr^{4+} in HEPES buffer at pH 7–8, the radiolabeling yield of [^{89}Zr]Mn$_3$O$_4$@PEG was then determined at different time intervals through radio-thin layer chromatography (radio-TLC), wherein [^{89}Zr]Mn$_3$O$_4$@PEG (R$_f$ = 0) could easily be distinguished from free ^{89}Zr (R$_f$ = 0.93) (Fig. 3(b)). The radiolabeling yield of [^{89}Zr]Mn$_3$O$_4$@PEG was found to be over 78% within the first 30 min, and kept slightly increasing after 180 min of incubation (Fig. 3(a), black line). As expected, ^{89}Zr-labeling was also concentration and temperature dependent, with higher concentration and higher incubation temperatures gaving higher labeling yield (Figs. 3(a and c)).

To further investigate the stability of ^{89}Zr labeling *in vitro* and the feasibility for *in vivo* applications, a serum stability study of the [^{89}Zr]Mn$_3$O$_4$@PEG NPs was subsequently conducted. After incubation in complete mouse serum at 37 °C for 48 h, nearly 67% of ^{89}Zr remained on the Mn$_3$O$_4$@PEG NPs, suggesting good stability of the radiolabeling on the Mn$_3$O$_4$@PEG NPs. Good radiostability in serum indicated that [^{89}Zr]Mn$_3$O$_4$@PEG NPs would have desirable properties *in vivo*.

In Vitro Biocompatibility Studies of Mn$_3$O$_4$@PEG NPs

The cytotoxicity of Mn$_3$O$_4$@PEG NPs was evaluated by a CCK-8 assay with normal cells (HEK-293) and tumor cells (SGC-7901). The concentration-dependent effect of

Mn$_3$O$_4$ conjugated NPs on the cell viability for 24 h and 48 h was determined. No obvious cytotoxicity of Mn$_3$O$_4$@PEG NPs to HEK-293 and SGC-7901 cells was observed at any studied concentration (from 0.2 to 1 mg mL^{-1}, Fig. 4). Even at the concentration of 1 mg mL^{-1}, the viability for both HEK-293 and SGC-7901 cells still remained above 80%, indicating that the Mn$_3$O$_4$@PEG NPs should have little cytotoxicity at the given concentration range.

In Vivo PET/MRI Imaging and Biodistribution Studies

As we all know, driven by the impending clinical requirement, the perfect combination of PET and MRI has been current under rapid development in clinical cancer detection and diagnosis due to its very high sensitivity of PET and ultra-high spatial resolution of MRI.[4, 5] To validate the feasibility of [^{89}Zr]Mn$_3$O$_4$@PEG NPs for dual-modality PET/MRI imaging and to investigate their biodistribution pattern *in vivo*, [^{89}Zr]Mn$_3$O$_4$@PEG NPs (200 μL, 2.7 MBq) were intravenously injected into healthy BALB/c mice. According to our previously reported method,[37] time points of 0.5, 2, 24 and 48 h p.i. were chosen for serial PET scans, as seen in Figure 5(a). Since the hydrodynamic diameters of [^{89}Zr]Mn$_3$O$_4$@PEG NPs are above the cut-off for renal filtration,[41] the route of clearance was mainly through the hepatobiliary pathway for these nanoparticles. Because of this, strong uptake of [^{89}Zr]Mn$_3$O$_4$@PEG NPs in the liver was observed, at 36.8 ± 2.3, 32.3 ± 1.8, 28.7 ± 0.8 and 25.6 ± 0.3 %ID/g at 0.5, 2, 24, and 48 h p.i. respectively, while the spleen radioactivity was also 23.4 ± 0.3, 28.9 ± 0.5, 32.5 ± 0.2, and 37.1 ± 0.3 %ID/g at 0.5, 2, 24, and 48 h p.i. respectively ($n = 3$). While PET imaging provides high sensitivity and quantitative tracking of radiotracers, essential anatomical information is also indispensable for accurate determination of the biodistribution patterns of [^{89}Zr]Mn$_3$O$_4$@PEG. Biodistribution studies of [^{89}Zr]Mn$_3$O$_4$@PEG NPs were also conducted at 48 h p.i. to validate the PET results. Dominant uptake
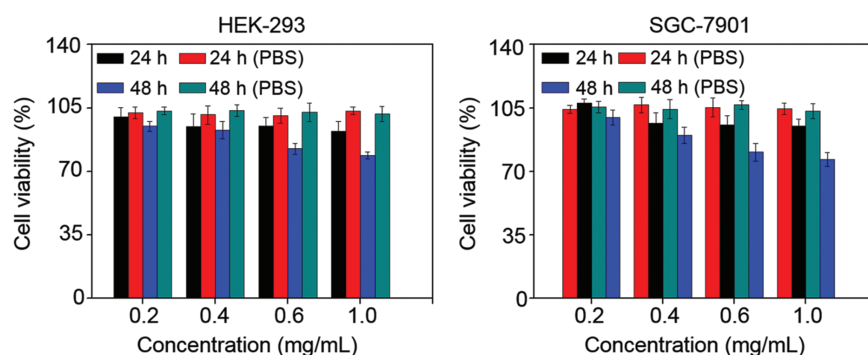
Figure 4. Viability of human embryonic kidney 293 cells (HEK-293) and human gastric cells (SGC-7901) incubated with Mn$_3$O$_4$@PEG NPs at different particle concentrations for 24 and 48 h. Black and blue bars indicate incubation with NPs, while red and green are controls.

of [^{89}Zr]Mn$_3$O$_4$@PEG NPs by both the liver and spleen was observed, which confirmed that the serial *in vivo* PET imaging accurately reflected the distribution pattern of [^{89}Zr]Mn$_3$O$_4$@PEG NPs in mice. To further supplement the PET results, MRI with high spatial resolution was used to investigate the Mn$_3$O$_4$@PEG NPs in BALB/c mice. As the Mn$_3$O$_4$@PEG NPs exhibited significant T_1 signal enhancement *in vitro*. *In vivo* T_1 MR imaging of BALB/c mice was conducted before and after intravenous injection of the Mn$_3$O$_4$@PEG NPs at a dose of 20 mg/kg NPs. Since the r_1 value of the Mn$_3$O$_4$@PEG NPs was calculated as 0.58 mM^{-1}s^{-1}, the injection dose was adequate for *in vivo* MR imaging. In view of this, a positive T_1 signal enhancement in the liver was observed at 0.5 h and 2 h post-injection of Mn$_3$O$_4$@PEG NPs. However, the

signal enhancement in the liver was decreased at 24 h, which could be attributed to the biodegradation and clearance of the NPs (Fig. 5(b)). Moreover, no detectable signal change for the kidney, compared with the same mice prior to the injection of the NPs. In order to further quantify the consistencey between the PET and MRI, by extracting the region of interest (ROI) of MRI and compared with the PET, the ROI of PET and MRI was all gradually decreasing at 0.5 h, 2 h and 24 h. This positive correlation between PET and MRI further proved the feasibility of [^{89}Zr]Mn$_3$O$_4$@PEG NPs for dual-modality PET/MR imaging.

In Vivo PET/MRI Imaging of Lymph Node Mapping

The lymphatic system plays a vital role in resisting disease invasion, and is also a common site for tumor metastasis. Therefore, precise identification of sentinel lymph nodes is of vital importance in both the prediction of cancer metastasis as well as determination of treatment options. Considering the [^{89}Zr]Mn$_3$O$_4$@PEG NPs as good dual-modality PET/MRI agent in biodistribution pattern *in vivo*, as a proof-of-concept, [^{89}Zr]Mn$_3$O$_4$@PEG NPs were then used as non-invasive dual-modality PET/MRI probes for lymph node mapping. After [^{89}Zr]Mn$_3$O$_4$@PEG NPs were subcutaneously injected into the left foot of normal healthy BALB/c mice (50 μL, 1.0 mM of Mn, $\sim$60 μCi), serial PET scans were carried out. As seen from Figure 6(a), accumulation of [^{89}Zr]Mn$_3$O$_4$@PEG NPs in the popliteal lymph node could clearly be seen at 0.5 h, 2 h and 6 h post-injection (red arrows), with the uptake of [^{89}Zr]Mn$_3$O$_4$@PEG NPs evaluated to be 7.7 ± 1.3, 15.3 ± 3.6, and 10.5 ± 2.4 %ID g^{-1}, respectively ($n = 3$) (Fig. 6(b)). On the contrary, the accumulation of [^{89}Zr]Mn$_3$O$_4$@PEG NPs in paws showed gradual and prominent decreasing after injection of NPs. Meanwhile, the main organ uptake of [89Zr]Mn$_3$O$_4$@PEG NPs *in vivo* at different time points were also carried out. As seen in Figure 6(b), there was no obvious accumulation such as heart, liver, spleen, lung, kidney, and so
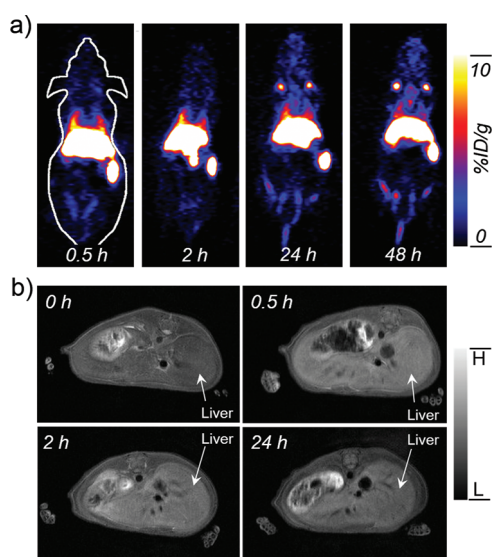
Figure 5. *In vivo* PET/MR imaging of [^{89}Zr]Mn$_3$O$_4$@PEG NPs. (a) Serial *in vivo* PET imaging of [^{89}Zr]Mn$_3$O$_4$@PEG in BALB/c mice at different post-injection time points; (b) Serial *in vivo* MR imaging of Mn$_3$O$_4$@PEG in BALB/c mice at different post-injection time points ($n = 3$ per group).
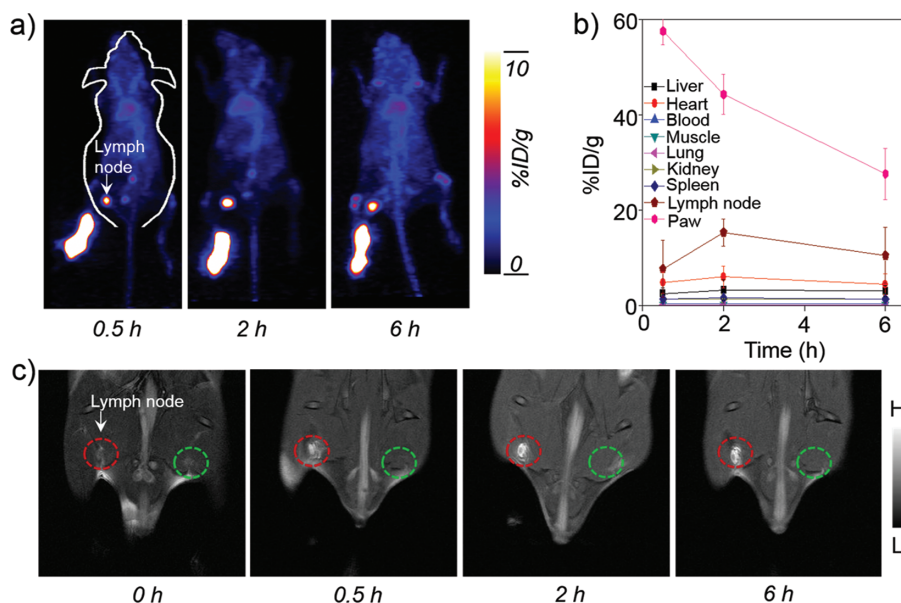
Figure 6. *In vivo* PET/MR imaging of lymph nodes with $[^{89}Zr]Mn_3O_4$@PEG NPs. (a) *In vivo* PET imaging acquired after subcutaneous injection of $[^{89}Zr]Mn_3O_4$@PEG NPs into the left footpad of the mouse ($n = 3$). Lymph nodes are indicated by arrows. (b) Quantification of the $[^{89}Zr]Mn_3O_4$@PEG NPs uptake by the lymph node, paw, heart, liver, kidney, blood, lung, muscle and spleen ($n = 3$). (c) *In vivo* MR imaging of the lymph nodes before and after injection of Mn_3O_4@PEG NPs into the left footpad of the mouse ($n = 3$). Lymph nodes are indicated by circles.

on, which was compared with the lymph nodes. The above results further revealed that the accumulation of $[^{89}Zr]Mn_3O_4$@PEG NPs in lymph nodes after injection was primarily due to the small size, which is well suited to uptake by the lymphatics.

Meanwhile, the accumulation of Mn_3O_4@PEG NPs in the sentinel lymph node could also be visualized by MRI, which showed gradual and prominent brightening of the lymph node after injection of Mn_3O_4@PEG NPs (50 μL, 1.0 mM of Mn; Fig. 6(c), red circle). As an internal contrast, the contralateral lymph node (Fig. 6(c), green circle) exhibited no obvious T_1 contrast enhancement at all the same time points observed. In order to further testify the consistencey between the PET and MRI, by extracting the region of interest (ROI) of MRI and PET, the ROI of PET and MRI was all gradually increasing at 0.5 h and 2 h, whereas the signal was then decreased at 6 h respectively. This positive correlation between PET and MRI further proved the feasibility of $[^{89}Zr]Mn_3O_4$@PEG NPs for dual-modality PET/MRI of lymph node mapping. Meanwhile, the *ex vivo* biodistribution of $[^{89}Zr]Mn_3O_4$@PEG NPs was also further investigated at 6 h post-injection, and verified a dominant uptake of NPs in the lymph node. Moreover, once the lymph node was located by the PET/MRI images, the area of the lymph node was further dissected for histological analysis. No apparent histological changes, such as lymphocytes, macrophages, neutrophils, and eosinophils, were observed by hematoxylin and eosin (H&E) staining. While the PET/MRI imaging presented herein could only

be acquired separately due to the lack of an integrated microPET/microMRI scanner, $[^{89}Zr]Mn_3O_4$@PEG NPs offer huge potential for future cancer patient diagnosis. Meanwhile, through further conjugation with other specific targeting ligands, $[^{89}Zr]Mn_3O_4$@PEG NPs could be additionally improved to enable accurate early diagnosis and targeted radiotherapy of cancers simultaneously.

In Vivo Biocompatibility Studies of Mn_3O_4@PEG NPs

To investigate the potential *in vivo* toxicity of Mn_3O_4@PEG NPs, histological assessment was carried out by injecting Mn_3O_4@PEG NPs (20 mg/kg) in healthy BALB/c mice via the tail vein. PBS injections served as the control. Two weeks after injection, mice were sacrificed and major organs (heart, liver, spleen, lung, and kidneys) of mice were sliced and stained by H&E for histology analysis. As shown in Figure 7, no noticeable tissue or cellular damage was observed in all major organs of mice, as compared to those obtained from the control group. There was no hydropic degeneration of cardiac muscle tissue in the heart samples. Normal liver macrophages also showed no evidence of inflammatory infiltrates. Meanwhile, there was no pathological changes and pulmonary fibrosis in the spleen and lung samples. Moreover, the glomerulus structure could be distinguished easily in the kidney samples. For further quantitative evaluation, serum biochemistry assays were then also conducted to investigate the influence of Mn_3O_4@PEG NPs, especially on potential hepatic injury
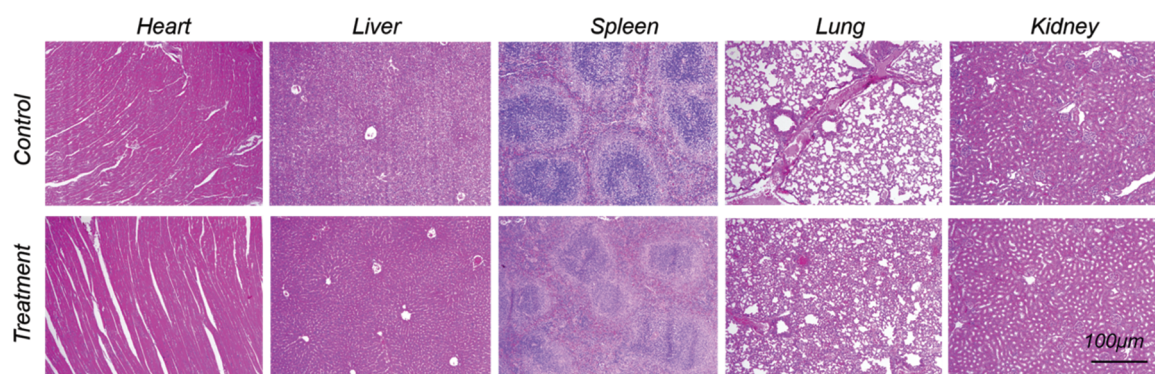
Figure 7. *In vivo* biocompatibility studies of Mn_3O_4@PEG in healthy mice. H&E staining of major organs from mice after injecting of Mn_3O_4@PEG NPs (dose: 20 mg/kg) at 14 d post-injection. Healthy mice treated with PBS were used as the control ($n = 3$).
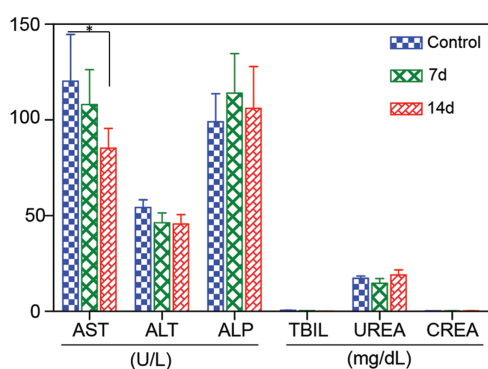
Figure 8. Serum biochemistry of liver and kidney function markers. Healthy BALB/c mice were intravenously injected with Mn_3O_4@PEG (dose: 20 mg kg^{-1}), and sacrificed on day 7 and day 14 post-injection ($n = 3$), the difference between AST in control and the treatment group on 14 days were statistically significant ($p < 0.05$).

and kidney functions (Fig. 8). Analysis of four primary hepatic function indicators including aspartate aminotransferase (AST), alanine aminotransferase (ALT), alkaline phosphatase (ALP), and total bilirubin (TBIL), as well as two kidney function indicators including serum creatinine (CREA) and serum urea (UREA), demonstrated no obvious hepatic or kidney disorders in both the mice treated with Mn_3O_4@PEG NPs and the control injected with PBS on both day 7 and day 14 post-injection. Although there was somewhat decreased in the level of ALT ($p < 0.05$) and AST on day 7 and day 14, as compared to those obtained from the control group, it was still within the normal range. These above results also suggested that Mn_3O_4@PEG NPs demonstrated no obvious toxicity in mice and may be a safe agent for biomedical imaging.

CONCLUSION

In conclusion, using Mn_3O_4 as a nanoplatform, we have developed a novel, efficient, chlealtor-free radiolabeling method to prepare the biocompatible T_1-MRI and PET contrast agent, $[^{89}Zr]Mn_3O_4$@PEG. Compared

to other prevalent Mn_3O_4-based NPs reported to date, $[^{89}Zr]Mn_3O_4$@PEG NPs make full use of the high sensitivity of PET and soft-tissue contrast of MRI. The utilization of $[^{89}Zr]Mn_3O_4$@PEG for *in vivo* dual-modality PET/MR imaging and lymph node mapping provide successful examples for future clinical applications.

Conflict of Interest
The authors confirm that there are no known conflicts of interest associated with this publication. Funding sources had no involvement in study design; collection, analysis, and interpretation of data; writing of the report; and in the decision to submit the article for publication.

REFERENCES
1. T. Su, Y. B. Wang, D. Han, J. Wang, S. Qi, L. Gao, Y. H. Shao, H. Y. Qiao, J. W. Chen, S. H. Liang, Y. Z. Nie, J. Y. Li, and F. Cao, Multimodality imaging of angiogenesis in a rabbit atherosclerotic model by GEBP11 peptide targeted nanoparticles. *Theranostics* 7, 4791 (**2017**).
2. T. Su, Y. Wang, J. Wang, D. Han, S. Ma, J. Cao, X. Li, R. Zhang, H. Qiao, J. Liang, G. Liu, B. Yang, S. Liang, Y. Nie, K. Wu, J. Li, and F. Cao. *In vivo* magnetic resonance and fluorescence dual-modality imaging of tumor angiogenesis in rats using GEBP11 peptide targeted magnetic nanoparticles. *J. Biomed. Nanotechnol.* 12, 1011 (**2016**).
3. C. Zamboglou, V. Drendel, C. A. Jilg, H. C. Rischke, T. I. Beck, W. Schultze-Seemann, T. Krauss, M. Mix, F. Schiller, U. Wetterauer, M. Werner, M. Langer, M. Bock, P. T. Meyer, and A. L. Grosu,

Comparison of ^{68}Ga-HBED-CC PSMA-PET/CT and multiparametric MRI for gross tumour volume detection in patients with primary prostate cancer based on slice by slice comparison with histopathology. *Theranostics* 7, 228 (**2017**).

4. B. Shen, D. Behera, M. L. James, S. T. Reyes, L. Andrews, P. W. Cipriano, M. Klukinov, A. B. Lutz, T. Mavlyutov, J. Rosenberg, A. E. Ruoho, C. R. McCurdy, S. S. Gambhir, D. C. Yeomans, S. Biswal, and F. T. Chin, Visualizing nerve injury in a neuropathic pain model with [18F]FTC-146 PET/MRI. *Theranostics* 7, 2794 (**2017**).

5. X. Li, J. Feng, R. Zhang, J. Wang, T. Su, Z. Tian, D. Han, C. Zhao, M. Fan, C. Li, B. Liu, X. Feng, Y. Nie, K. Wu, Y. Chen, H. Deng, and F. Cao, Quaternized chitosan/alginate-Fe$_3$O$_4$ magnetic nanoparticles enhance the chemosensitization of multidrug-resistant gastric carcinoma by regulating cell autophagy activity in mice. *J. Biomed. Nanotechnol.* 12, 948 (**2016**).

6. C. Glaus, R. Rossin, M. J. Welch, and G. Bao. *In vivo* evaluation of Cu-64-labeled magnetic nanoparticles as a dual-modality PET/MR imaging agent. *Bioconjugate. Chem.* 21, 715 (**2010**).

7. B. J. Pichler, A. Kolb, T. Nagele, and H. P. Schlemmer, PET/MRI: Paving the way for the next generation of clinical multimodality imaging applications. *J. Nucl. Med.* 51, 333 (**2010**).

8. J. Wang, W. Tao, X. Chen, O. C. Farokhzad, and G. Liu, Emerging advances in nanotheranostics with intelligent bioresponsive systems. *Theranostics* 7, 3915 (**2017**).

9. H. Lee, E. Lee, D. K. Kim, N. K. Jang, Y. Y. Jeong, and S. Jon, Antibiofouling polymer-coated superparamagnetic iron oxide nanoparticles as potential magnetic resonance contrast agents for *in vivo* cancer imaging. *J. Am. Chem. Soc.* 128, 7383 (**2006**).

10. L. L. Ma, M. D. Feldman, J. M. Tam, A. S. Paranjape, K. K. Cheruku, T. A. Larson, J. O. Tam, D. R. Ingram, V. Paramita, J. W. Villard, J. T. Jenkins, T. Wang, G. D. Clarke, R. Asmis, K. Sokolov, B. Chandrasekar, T. E. Milner, and K. P. Johnston, Small multifunctional nanoclusters (nanoroses) for targeted cellular imaging and therapy. *Acs Nano* 3, 2686 (**2009**).

11. R. M. Wong, D. A. Gilbert, K. Liu, and A. Y. Louie, Rapid size-controlled synthesis of dextran-coated, Cu-64-doped iron oxide nanoparticles. *Acs Nano* 6, 3461 (**2012**).

12. X. Q. Yang, H. Hong, J. J. Grailer, I. J. Rowland, A. Javadi, S. A. Hurley, Y. L. Xiao, Y. A. Yang, Y. Zhang, R. Nickles, W. B. Cai, D. A. Steeber, and S. Q. Gong, cRGD-functionalized, DOX-conjugatedd, and Cu-64-labeled superparamagnetic iron oxide nanoparticles for targeted anticancer drug delivery and PET/MR imaging. *Biomaterials* 32, 4151 (**2011**).

13. E. M. Shapiro and A. P. Koretsky, *Magnetic Resonance in Medicine* 60, 265 (**2008**).

14. H. B. Na, J. H. Lee, K. J. An, Y. I. Park, M. Park, I. S. Lee, D. H. Nam, S. T. Kim, S. H. Kim, S. W. Kim, K. H. Lim, K. S. Kim, S. O. Kim, and T. Hyeon, Development of a T-1 contrast agent for magnetic resonance imaging using MnO nanoparticles. *Angew. Chem. Int. Edit.* 46, 5397 (**2007**).

15. T. Yu, J. Moon, J. Park, Y. I. Park, H. B. Na, B. H. Kim, I. C. Song, W. K. Moon, and T. Hyeon, Various-shaped uniform Mn$_3$O$_4$ nanocrystals synthesized at low temperature in air atmosphere. *Chem. Mater.* 21, 2272 (**2009**).

16. Y. W. Jun, J. H. Lee, and J. Cheon, Chemical design of nanoparticle probes for high-performance magnetic resonance imaging. *Angew. Chem. Int. Edit.* 47, 5122 (**2008**).

17. M. F. Bennewitz, T. L. Lobo, M. K. Nkansah, G. Ulas, G. W. Brudvig, and E. M. Shapiro, Biocompatible and pH-sensitive PLGA encapsulated MnO nanocrystals for molecular and cellular MRI. *ACS Nano* 5, 3438 (**2011**).

18. T. L. Ha, H. J. Kim, J. Shin, G. H. Im, J. W. Lee, H. Heo, J. Yang, C. M. Kang, Y. S. Choe, J. H. Lee, and I. S. Lee, Development of target-specific multimodality imaging agent by using hollow manganese oxide nanoparticles as a platform. *Chem. Commun.* 47, 9176 (**2011**).

19. R. Hao, J. Yu, Y. L. Hou, and S. H. Sun, One-pot synthesis of hollow/porous Mn-based nanoparticles via a controlled ion transfer process. *Chem. Commun.* 47, 9095 (**2011**).

20. J. M. Shin, R. M. Anisur, M. K. Ko, G. H. Im, J. H. Lee, and I. S. Lee, Hollow manganese oxide nanoparticles as multifunctional agents for magnetic resonance imaging and drug delivery. *Angew. Chem. Int. Edit.* 48, 321 (**2009**).

21. C. C. Huang, N. H. Khu, and C. S. Yeh, The characteristics of sub 10 nm manganese oxide T-1 contrast agents of different nanostructured morphologies. *Biomaterials* 31, 4073 (**2010**).

22. J. Huang, J. Xie, K. Chen, L. H. Bu, S. Lee, Z. Cheng, X. G. Li, and X. Y. Chen, HSA coated MnO nanoparticles with prominent MRI contrast for tumor imaging. *Chem. Commun.* 46, 6684 (**2010**).

23. X. Y. Yang, Z. G. Zhou, L. Wang, C. Z. Tang, H. Yang, and S. P. Yang, Folate conjugatedd Mn$_3$O$_4$@SiO$_2$ nanoparticles for targeted magnetic resonance imaging *in vivo*. *Mater. Res. Bull.* 57, 97 (**2014**).

24. H. Hu, A. T. Dai, J. Sun, X. Y. Li, F. H. Gao, L. Z. Wu, Y. Fang, H. Yang, L. An, H. X. Wu, and S. P. Yang, Aptamer-conjugatedd Mn$_3$O$_4$@SiO$_2$ core–shell nanoprobes for targeted magnetic resonance imaging. *Nanoscale* 5, 10447 (**2013**).

25. H. Yang, Y. M. Zhuang, H. Hu, X. X. Du, C. X. Zhang, X. Y. Shi, H. X. Wu, and S. P. Yang, Silica-coated manganese oxide nanoparticles as a platform for targeted magnetic resonance and fluorescence imaging of cancer cells. *Adv. Funct. Mater.* 20, 1733 (**2010**).

26. A. Ranganathan, J. Campo, J. Myerson, V. Shuvaev, B. Zern, V. Muzykantov, and D. M. Eckmann, Fluorescence microscopy imaging calibration for quantifying nanocarrier binding to cells during shear flow exposure. *J. Biomed. Nanotechnol.* 13, 737 (**2017**).

27. N. Li, T. Li, C. Liu, S. Ye, J. Liang, and H. Han, Folic acid-targeted and cell penetrating peptide-mediated theranostic nanoplatform for high-efficiency tri-modal imaging-guided synergistic anticancer phototherapy. *J. Biomed. Nanotechnol.* 12, 878 (**2016**).

28. L. Cheng, S. Shen, D. Jiang, Q. Jin, P. A. Ellison, E. B. Ehlerding, S. Goel, G. Song, P. Huang, T. E. Barnhart, Z. Liu, and W. Cai, Chelator-free labeling of metal oxide nanostructures with zirconium-89 for positron emission tomography imaging. *ACS Nano* 11, 12193 (**2017**).

29. Y. Wang, Y. Liu, H. Luehmann, X. Xia, P. Brown, C. Jarreau, M. Welch, and Y. Xia, Evaluating the pharmacokinetics and *in vivo* cancer targeting capability of Au nanocages by positron emission tomography imaging. *ACS Nano* 6, 5880 (**2012**).

30. H. J. Aerts, L. Dubois, L. Perk, P. Vermaelen, G. A. van Dongen, B. G. Wouters, and P. Lambin, Disparity between *in vivo* EGFR expression and 89Zr-labeled cetuximab uptake assessed with PET. *J. Nucl. Med.* 50, 123 (**2009**).

31. J. N. Tinianow, H. S. Gill, A. Ogasawara, J. E. Flores, A. N. Vanderbilt, E. Luis, R. Vandlen, M. Darwish, J. R. Junutula, and S.-P. Williams, Site-specifically 89 Zr-labeled monoclonal antibodies for ImmunoPET. *Nucl. Med. Biol.* 37, 289 (**2010**).

32. J. P. Holland, V. Divilov, N. H. Bander, P. M. Smith-Jones, S. M. Larson, and J. S. Lewis, 89Zr-DFO-J591 for immunoPET of prostate-specific membrane antigen expression *in vivo*. *J. Nucl. Med.* 51, 1293 (**2010**).

33. L. Cheng, K. Yang, Q. Chen, and Z. Liu, Organic stealth nanoparticles for highly effective *in vivo* near-infrared photothermal therapy of cancer. *ACS Nano* 6, 5605 (**2012**).

34. M. Zhou, R. Zhang, M. Huang, W. Lu, S. Song, M. P. Melancon, M. Tian, D. Liang, and C. Li, A chelator-free multifunctional [64Cu]CuS nanoparticle platform for simultaneous micro-PET/CT imaging and photothermal ablation therapy. *J. Am. Chem. Soc.* 132, 15351 (**2010**).

35. F. Chen, P. A. Ellison, C. M. Lewis, H. Hong, Y. Zhang, S. Shi, R. Hernandez, M. E. Meyerand, T. E. Barnhart, and W. Cai, Chelator-free synthesis of a dual-modality PET/MRI agent. *Angew. Chem. Int. Edit.* 52, 13319 (**2013**).

36. R. Chakravarty, H. F. Valdovinos, F. Chen, C. M. Lewis, P. A. Ellison, H. Luo, M. E. Meyerand, R. J. Nickles, and W. Cai,

Intrinsically germanium-69-labeled iron oxide nanoparticles: Synthesis and *in-vivo* dual-modality PET/MR imaging. *Adv. Mater.* 26, 5119 (**2014**).

37. F. Chen, S. Goel, H. F. Valdovinos, H. Luo, R. Hernandez, T. E. Barnhart, and W. Cai. *In vivo* integrity and biological fate of chelator-free zirconium-89-labeled mesoporous silica nanoparticles. *ACS Nano* 9, 7950 (**2015**).

38. Y. Zhan, F. Ai, F. Chen, H. F. Valdovinos, H. Orbay, H. Sun, J. Liang, T. E. Barnhart, J. Tian, and W. Cai, Intrinsically zirconium-89 labeled Gd$_2$O$_2$S: Eu nanoprobes for *in vivo* positron emission tomography and gamma-ray-induced radioluminescence imaging. *Small* 12, 2872 (**2016**).

39. F. Ai, S. Goel, Y. Zhan, H. F. Valdovinos, F. Chen, T. E. Barnhart, and W. Cai, Intrinsically 89Zr-labeled Gd$_2$O$_2$S: Eu nanophosphors with high *in vivo* stability for dual-modality imaging. *Am. J. Transl. Res.* 8, 5591 (**2016**).

40. L. Cheng, A. Kamkaew, S. Shen, H. F. Valdovinos, H. Sun, R. Hernandez, S. Goel, T. Liu, C. R. Thompson, and T. E. Barnhart, Facile preparation of multifunctional WS2/WOx nanodots for chelator-free 89Zr-labeling and in vivo PET imaging. *Small* 12, 5750 (**2016**).

41. H. S. Choi, W. Liu, P. Misra, E. Tanaka, J. P. Zimmer, B. I. Ipe, M. G. Bawendi, and J. V. Frangioni, Renal clearance of quantum dots. *Nat. Biotechnol.* 25, 1165 (**2007**).